Homogenised Optoelectronic Properties in Perovskites: Achieving High-Efficiency Solar Cells with Common Chloride Additives

Junke Wang,[#] Shuaifeng Hu,[#] Xinyu Gu,[#] Minh Anh Truong,[#] Yi Yang,[#] Cheng Liu, Gunnar Kusch, Zhongcheng Yuan, Manuel Kober-Czerny, Zuhong Zhang, Zhenhuang Su, Kyohei Nakano, Akash Dasgupta, Xianfu Zhang, Xinyi Shen, Nobutaka Shioya, Noriko Kurose, Daichi Shirakura, Zaiwei Wang, Wei Zhou, Meng Li, Takeshi Hasegawa, Xingyu Gao, Keisuke Tajima, Rachel A. Oliver, Yixin Zhao, Zhijun Ning,[*] Atsushi Wakamiya,[*] Henry J. Snaith,[*] and Hao Chen[*]

Abstract

Improving the bulk quality of perovskite films is critical for achieving higher-performance photovoltaic devices. Chloride-containing additives, including lead chloride ($PbCl_2$) and methylammonium chloride (MACl)—standard additives widely adopted in perovskite photovoltaics—are effective for controlling crystallisation kinetics and grain morphology. However, the distinct impacts of different forms of chloride additives on nanoscale phase uniformity and luminescence homogeneity remains underexplored. Here, we provide new insights into how the choice and combination of chloride additives influence phase transitions and spatially uniform carrier dynamics within perovskite films. We demonstrate that strategically combining MACl and $PbCl_2$ improves crystallinity and optoelectronic uniformity across dimensions spanning micrometres to millimetres. Leveraging these findings, we fabricated inverted (p-i-n) perovskite solar cells achieving certified quasi-steady-state efficiencies of 26.4% and 24.5% at device areas of 0.05 and 1 cm^2, respectively. Furthermore, these devices exhibit robust operational stability, retaining 88% of their initial performance after 1200 hours of continuous maximum power point tracking at elevated temperatures (65 °C) under simulated AM1.5G illumination. Our results elucidate the mechanistic differences between chloride additive forms, providing a viable strategy for advancing large-area, high-efficiency, and thermally stable perovskite photovoltaics.

Introduction

Metal-halide perovskites are semiconductor materials that can be fabricated via cost-effective solution-[1,2] or vacuum-based[3,4] methods. Their remarkable optoelectronic properties[5,6] have positioned them as promising candidates for photovoltaic devices capable of efficiently converting sunlight into electricity[7]. In

the past decade, substantial progress has been achieved in single-junction perovskite solar cells (PSCs), with power conversion efficiencies (PCEs) now exceeding 27%[8-11]—comparable to those of state-of-the-art silicon solar cells[12,13].

Significant advancements in PSC performance have primarily resulted from reduced interfacial losses[14-19], achieved through mitigating defect sites at perovskite heterojunctions and minimising nonradiative recombination losses[20-25]. To further enhance device performance, precise control over local composition and optoelectronic uniformity within the perovskite absorber is essential[26-30]. Recent studies have highlighted that inhomogeneous phase distributions from micro- to millimetre scales are detrimental to device efficiency and stability, particularly when upscaling to larger areas[31-34]. Within solution-processing methods, achieving balanced crystallisation among mixed-cation and mixed-anion components is critical to improve phase homogeneity[30,35]. Chloride-based additives have been proven effective for controlling crystallisation kinetics and improving the semiconductor quality of perovskite films[6,36-40]; however, their influence on local optoelectronic uniformity remains insufficiently understood.

Here, we investigate the influence of different forms of chloride additives on the phase distribution and optoelectronic uniformity in perovskite films. By comparatively evaluating two widely adopted chloride additives[18]—methylammonium chloride (MACl) and lead chloride ($PbCl_2$)—we confirm that chloride incorporation notably accelerates the transition from the inactive yellow phase to the active black perovskite phase. We observe that MACl promotes the out-of-plane compositional heterogeneity, resulting in variable carrier dynamics at micrometre scales. In contrast, $PbCl_2$ more effectively incorporates chloride uniformly within grain interiors, homogenising local optoelectronic properties but introducing detrimental lead iodide (PbI_2) grains that hinder charge transport. We demonstrate that a synergistic combination of MACl and $PbCl_2$ significantly improves overall film crystallinity and achieves spatially homogeneous carrier dynamics from microscale to millimetre-scale dimensions. Consequently, we fabricate inverted (p-i-n) PSCs that achieve efficiencies of up to 27.0% (certified 26.4%) at an active areas of approximately 0.05 cm^2, and 25.5% (certified 24.5) at 1-cm^2. These devices retain 88% of their initial PCE after 1200 hours of continuous maximum power point tracking (MPPT) under simulated AM1.5G illumination at about 65 °C. Although the chloride-assisted crystallisation and the transition from yellow to black perovskite phases using MACl or $PbCl_2$ are well-

documented, our study provides a systematic investigation into their distinct impacts on compositional and morphological uniformity at both micrometre and millimetre scales. We demonstrate how these pathways govern local phase and luminescence homogeneity, as well as carrier dynamics, offering a mechanistic understanding of how high-efficiency and stable perovskite photovoltaics can be achieved using widely accessible and commonly utilised chloride additives.

Results

Phase transition of chloride-engineered perovskites

We prepared perovskite films with an initial composition of $Cs_{0.05}FA_{0.90}MA_{0.05}PbI_3$ (FA: formamidinium) using solution processing as control samples. To study the mechanism of chloride incorporation, we fabricated films with chloride additives: MACl (13 mol%), $PbCl_2$ (3 mol%), and their combination (13 mol% MACl + 3 mol % $PbCl_2$, relative to PbI_2) after initial device optimisation (**Supplementary Fig. 1–2**). Synchrotron radiation-based in-situ grazing incidence wide-angle X-ray scattering (GIWAXS) was employed to track film crystallisation during spin coating and subsequent annealing (**Fig. 1a**). In the initial stage of spin coating (0 to 40 seconds), we observe two distinct diffraction peaks at scattering vectors (q) of 5.3 and 7.3 nm^{-1} regardless of using chloride additives, indicating low-dimensional intermediate phases composed of lead iodide-centred adducts with a specific number of solvent molecules or FAI-rich perovskite compounds[41-43]. Upon initiating antisolvent dripping at around 40 seconds, an additional diffraction peak emerges at q = 8.4 nm^{-1}. Subsequently, as annealing commenced at around 60 s, a new diffraction develops at q = 10 nm^{-1}. The diffraction peaks at 8.4 and 10 nm^{-1} represent the hexagonal 2H polytype (yellow δ-phase) and the black 3D perovskite phase, respectively[41]. Notably, the control sample exhibits incomplete conversion from the yellow to the black phase, maintaining strong diffraction intensity of the 2H phase even after 150 seconds at 150 °C. In contrast, samples incorporating chloride additives display significantly reduced intensity and a shorter duration of the 2H phase, completely eliminating the peak at 8.4 nm^{-1} within 60 seconds at 120 °C. We propose that the suppressed retention of the yellow 2H polytype is due to a kinetic effect introduced by chloride-containing additives. In the precursor stage, chloride ions can bind to the surfaces of the emerging face-sharing 2H crystallites[44,45]. Following antisolvent dripping, the chloride ions that coordinate with Pb^{2+} ions at the octahedral terminal corners destabilise the face-sharing

polytype and promote the formation of corner-sharing 3D-like structures. The resulting seeding layer facilitates the complete conversion of black 3D phases in the bulk material. The trends in the 3D structure conversion rate are consistent with in-situ photoluminescence (PL) measurements, in which the MACl + $PbCl_2$ film shows the fastest redshift and the highest 3D peak emission intensity, even without thermal annealing[46] (**Supplementary Fig. 3–4)**. Interestingly, the film containing the combination of MACl and $PbCl_2$ (hereafter denoted as MACl + $PbCl_2$) maintains intermediate phases ($q \leq 7.3$ nm^{-1}) throughout annealing up to 300 seconds, similar to the control film. Conversely, films with only MACl or $PbCl_2$ show reduced presence of these solvent-involved intermediate phases. Preserving intermediate phases while facilitating rapid δ-phase conversion can positively impact the crystallisation pathway, leading to higher-quality perovskite crystals[42]. Ex-situ GIWAXS measurements further assess the crystallinity of annealed perovskite films (**Fig. 1b**). We observe no low-dimensional phases in any films after annealing. Films containing MACl, particularly those with MACl + $PbCl_2$, exhibit a significantly enhanced (100) diffraction intensities in both in-plane (Q_{xy}) and out-of-plane (Q_z) directions compared to the control film. In contrast, $PbCl_2$ alone provides limited improvement in crystallinity and promotes the undesirable formation of PbI_2 residue (q = 0.9 $Å^{-1}$) [47-49]. These crystallographic analyses confirm that chloride additives universally facilitate the formation of the desired 3D perovskite phase. Importantly, combining MACl and $PbCl_2$ effectively preserves intermediate phases for an optimal duration, resulting in superior crystallinity of the final perovskite films (**Supplementary Fig. 5–6**, **Supplementary Table 1**).

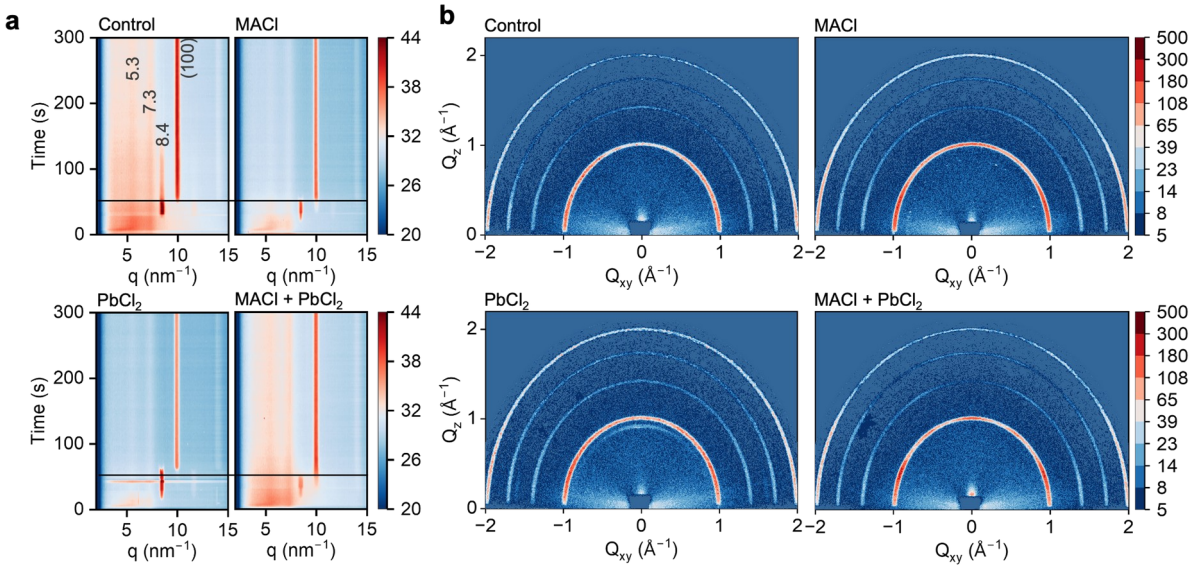

Fig. 1 Film crystallization process. a, In-situ (ψ = 0.4°) and **b**, ex-situ (ψ = 0.4°) 2D GIWAXS patterns for the control, MACl, $PbCl_2$, and MACl + $PbCl_2$ samples. For the in-situ measurements, the films are deposited on glass substrates in ambient air. The control sample is annealed at 150 °C for a full phase conversion and other samples are annealed at 120 °C. All films for ex-situ GIWAXS measurements are deposited under inert conditions with an annealing temperature of 120 °C.

Phase distribution and nanoscale optical properties

Following the crystallographic analysis, we investigate the influence of additives on phase distribution using time-of-flight secondary ion mass spectroscopy (ToF-SIMS). The perovskite film incorporating 3 mol% $PbCl_2$ exhibits a notably higher chloride content than the film containing 13 mol% MACl (**Fig. 2a** and **Supplementary Fig. 7–8**). This corresponds to a slight increase (~20 meV) in the photovoltaic bandgap (**Supplementary Fig. 9**), likely reflecting the efficient integration of $PbCl_2$ into the perovskite grain interiors[50]. Moreover, 3D tomographic analysis of the $PbCl_2$-modified film reveals a uniform chloride distribution throughout its bulk (**Fig. 2b**). Conversely, the MACl-containing film displays pronounced chloride accumulation near the buried interface and enrichment of MA cations toward the top surface (**Fig. 2c**). This coincides with a modest increase in Cs^+ at the bottom interface and I^- at the top surface, respectively, which may help retain local electroneutrality in the bulk film (**Supplementary Fig. 10**). We believe this phenomenon is due to the volatility of MACl during annealing. Chloride-containing species near the surface can escape more easily, while those deeper in the film are kinetically trapped[51], leading to an apparent enrichment at the bottom. At the same time, MA-related species from both the MAI precursor and MACl additive can redistribute and are only partially vaporised, leaving some residual MA near the surface after annealing. These observations indicate that MACl is relatively inefficient at incorporating chloride within perovskite grains, resulting in significant compositional inhomogeneity. Additionally, we recognise that the chemical depth profile is sensitive to precursor stoichiometry and processing conditions. Changes in the intermediate adduct phases during antisolvent quenching and the redistribution of volatile species, such as MACl, during thermal annealing may lead to different apparent ion distributions[52].

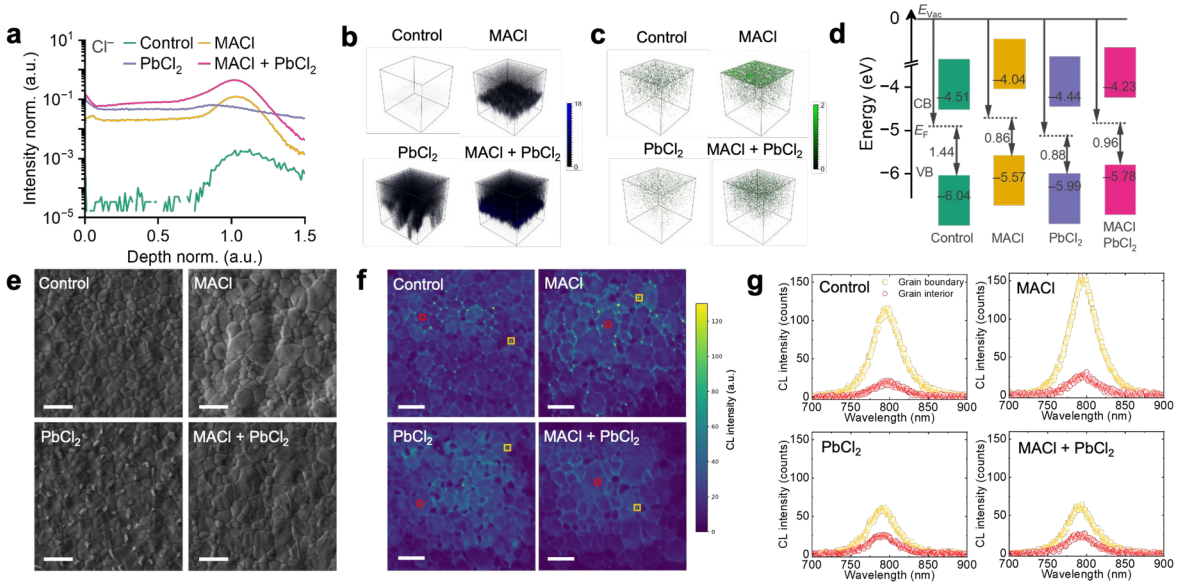

Fig. 2 Phase distribution and nanoscopic emission of perovskite films. a, ToF-SIMS depth profiles of chloride anions. 3D tomography of **b**, chloride anion and **c**, MA cation. **d**, Energy level diagram generated from the UPS spectra of perovskite films fabricated without (control) and with additives. **e**, SEM, **f**, CL emission intensity images, and **g**, CL spectra of grain boundary (yellow square) and grain interior (red circle) regions of perovskite films fabricated without (control) and with additives. Scale bars in **e** and **f** are 1 μm. More CL spectra from 10 different pixels are shown in **Supplementary Fig. 14**.

We further analyse the surface electronic structure using ultraviolet photoelectron spectroscopy (UPS, **Fig. 2d** and **Supplementary Fig. 11**). Compared to the control films, we identify the largest upward shift (0.47 eV) in the valence band maximum (VBM) for the MACl-containing films, followed by a smaller shift (0.26 eV) in the MACl + $PbCl_2$ films. The $PbCl_2$ film shows negligible shifts near the band edges. Correlating with the ToF-SIMS data, we attribute the pronounced VBM shift primarily to surface accumulation of MA cations, which lowers the ionisation energy. Additionally, we observe a decreased offset between the Fermi level (E_F) and VBM in all chloride-engineered films, suggesting the formation of a more intrinsic, electronically neutral top surface. Based on the measured photovoltaic bandgap values, we estimate the conduction band minimum (CBM) to be –4.51, –4.04, –4.44, and –4.23 eV for the control, MACl-, $PbCl_2$-, and MACl + $PbCl_2$-added films, respectively. Considering the lowest unoccupied molecular orbital (LUMO) energy level (–4.20 eV) of the electron transport layer (ETL) C_{60}[53], the film modified with MACl + $PbCl_2$ presents the smallest interfacial energy mismatch on the electron extraction side.

To correlate film morphology with optical emission properties, we perform scanning electron microscopy (SEM) coupled with cathodoluminescence (CL) imaging at sub-micrometre resolution (**Fig. 2e−g**). Top-view SEM images show that chloride additives effectively increase the apparent average grain size from 298 ± 96 nm (control) to 318 ± 151 (MACl), 272 ± 108 ($PbCl_2$), and 412 ± 171 nm (MACl + $PbCl_2$) (**Supplementary Fig. 12**). Cross-sectional SEM images show that the film with only MACl has greater surface roughness due to the increased non-uniformity in grain morphology (**Supplementary Fig. 13**). Correspondingly, CL imaging under continuous electron beam excitation reveals distinct photon emission behaviours. For the control films, emission near 800 nm (associated with the 3D perovskite phase) is stronger at grain boundaries compared to grain interiors, observed across multiple grain regions (**Fig. 2f−g** and **Supplementary Fig. 14–16**). Interestingly, MACl-added films exhibit an even more pronounced contrast, with grain boundaries emitting up to six times higher intensity than the interiors. This observation is unexpected since grain boundaries generally harbour higher defect densities and are known as non-radiative recombination sites. However, we find no clear correlation between grain size and bulk non-radiative recombination rate, suggesting grain boundaries are not dominate in non-radiative recombination processes (**Supplementary Fig. 25**). Additionally, the overall averaged CL intensity and maximum emission wavelengths show minimal variations among the different samples (**Supplementary Fig. 17**), highlighting that the observed emission contrast is highly localised to grain boundaries. We rule out beam-induced halide segregation as a possible cause of brighter grain boundaries[54] since no energy shifts are detected between grain boundary and interior regions (**Fig. 2g** and **Supplementary Fig. 15–16**). While beam-induced degradation within the grain interiors may be a potential factor[55], we propose enhanced surface roughness from MACl incorporation increases scattering and optical out-coupling efficiency, contributing to greater local emission brightness[56,57].

In contrast, $PbCl_2$- and MACl + $PbCl_2$ films exihibit significantly narrower variations in CL emission intensity across grain boundaries and interiors. This enhanced uniformity in emission characteristics reflects improved morphological and optoelectronic homogeneity. However, $PbCl_2$-added films featured distinct needle-shaped features attributed to excess PbI_2, visible in CL maps filtered within the 510–550 nm spectral range (**Supplementary Fig. 18–20**). Combined with our ToF-SIMS analysis, these results indicate MACl alone promotes

morphological disorder and nonuniform optoelectronic properties, whereas $PbCl_2$ contributes to uniform emission properties but introduces unwanted PbI_2 phases. Ultimately, the combination of MACl and $PbCl_2$ additives provides a balanced approach, yielding highly uniform carrier dynamics across micrometre-scale regions.

Carrier dynamics of perovskite films and devices

We further investigate the carrier dynamics within perovskite films using time-resolved photoluminescence (TRPL) measurements. Consistent with our previous approach[58], we acquire four TRPL decay curves using two different excitation fluences (1.3×10^9 and 1.3×10^{10} cm^{-2} per pulse) on both the top and bottom surfaces of the perovskite samples (**Fig. 3a** and **Supplementary Fig. 21–24**). Employing a comprehensive physical model coupled with Bayesian inference, we extract eight device-relevant parameters, including the bulk and surface recombination velocities. We calculate the median bulk recombination rates to be 2.3×10^4, 7.1×10^3, 6.3×10^4, and 5.9×10^3 s^{-1} for the control, MACl, $PbCl_2$, and MACl + $PbCl_2$ samples, respectively. We interpret that improved film uniformity does not necessarily lead to a reduced average bulk recombination rate. While $PbCl_2$ facilitates more uniform chloride incorporation, it also promotes the formation of PbI_2 phases (**Supplementary Fig. 6 and 20**), which can introduce non-radiative recombination centres. Interestingly, the MACl + $PbCl_2$ condition balances these competing effects, resulting in highly crystalline, phase-pure films with homogeneous carrier dynamics and reduced non-radiative bulk recombination. In comparison, median surface recombination rates are found to be 9.2×10^5, 4.7×10^5, 1.4×10^6, and 1.2×10^6 s^{-1} for the control, MACl, $PbCl_2$, and MACl + $PbCl_2$ samples, respectively, suggesting a comparatively minor influence of chloride treatments on surface recombination processes (**Fig. 3b**). Additionally, we estimate the vertical charge-carrier mobility of the films, considering spectral changes caused by self-absorption during pulsed photoexcitation (**Methods** and **Supplementary Fig. 26**)[58,59]. Remarkably, the MACl + $PbCl_2$-modified film shows enhanced vertical mobility of 40.2 cm^2 V^{-1} s^{-1} compared to substantially lower values (0.6–2.0 cm^2 V^{-1} s^{-1}) in other films. Hence, the combined use of MACl and $PbCl_2$ considerably improves charge transport properties beneficial for photovoltaic applications.

We subsequently perform quasi-Fermi level splitting (QFLS) analysis via absolute PL to evaluate the intrinsic efficiency potential of perovskite films, without the

influence of series resistance losses (**Fig. 3c**). Comparing neat films processed on bare glass with those integrated into half-cells using NiO_X/[4-(3,6-dimethyl-9H-carbazol-9-yl)butyl]phosphonic acid (Me-4PACz) as the hole transport layer (HTL), we observe QFLS enhancements of 78 and 68 meV for the control and MACl + $PbCl_2$-modified films, respectively. Correspondingly, the implied open-circuit voltage (iV_{OC}) reaches 1.201 V in the control sample and 1.226 V in the MACl + $PbCl_2$ film, consistent with the passivation effect from the self-assembled monolayer[25] and suggests better optoelectronic quality for the latter samples. Interestingly, the subsequent deposition of a C_{60} layer (forming a p-i-n structure) tremendously reduces the iV_{OC} of the control sample to 1.143 V, whereas the MACl + $PbCl_2$ sample retains a much higher iV_{OC} of 1.191 V. Simultaneously, the control sample allows for a pseudo-fill factor (*p*FF) of 86.8%, compared with a higher 88.1% obtained for the MACl + $PbCl_2$ device. This indicates that the MACl + $PbCl_2$ additive reduces nonradiative recombination and restores fast charge extraction when in contact with a C_{60} layer atop[25]. Accordingly, pseudo-current density-voltage (*pJ*–*V*) characteristics imply efficiency potentials of 26.18% for control and 27.67% for MACl + $PbCl_2$-based device.

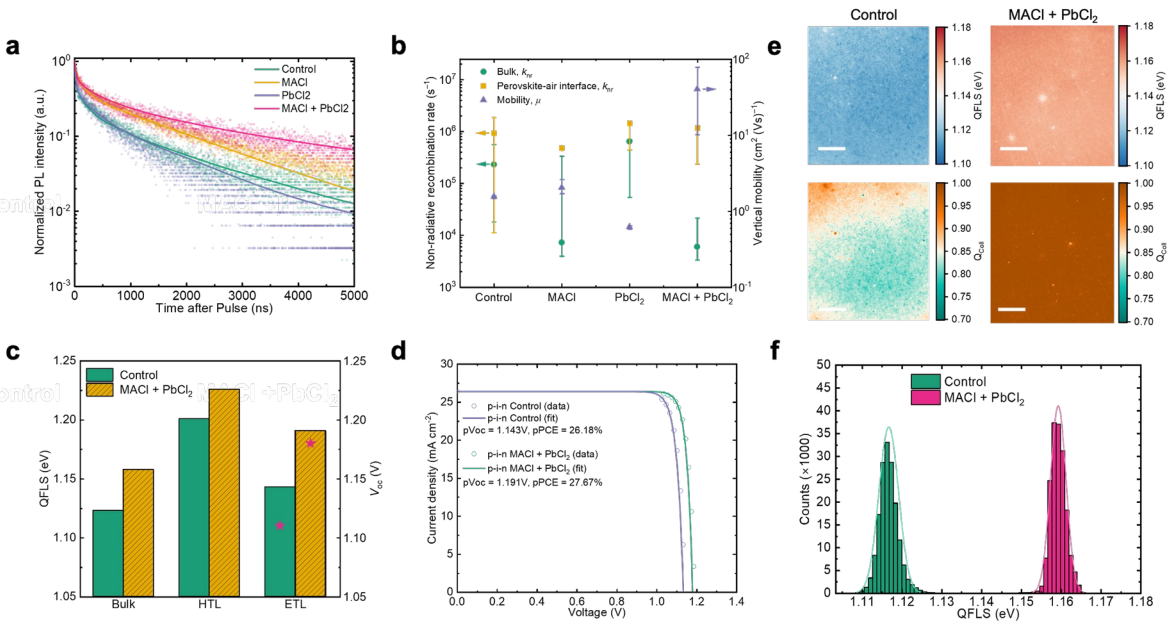

Fig. 3 Optoelectronic properties of perovskite films. a,**b**, Representative TRPL response (**a**), the inferred non-radiative bulk and surface recombination rate, and the vertical mobility (**b**) for the control, MACl, $PbCl_2$, and MACl + $PbCl_2$ perovskite deposited on glass/ITO/HTL substrates. For clarity, only one TRPL measured from the glass side is shown (excitation fluence 1.3 × 10^9 cm^{-2}). The fitted curves from our global inference are shown in **Supplementary Fig. 21–**

24. In **Fig. 3b**, the solid dots represent median inferred values and the error bars indicate the first and third quartiles. **c**, QFLS of control and MACl + $PbCl_2$ perovskite films deposited on bare glass, HTL half stack and p-i-n layout. The stars represent the measured device V_{OC} prepared in the same batch. **d**, Pseudo *J*–*V* characteristics of control and MACl + $PbCl_2$ films processed in a p-i-n layout. **e**, QFLS imaging recorded at V_{OC} conditions and the charge collection quality mapping by comparing the PLQY at V_{OC} and J_{SC} conditions for control and MACl + $PbCl_2$-added PSCs. The scale bars are 1 mm. **f**, QFLS histograms of samples displayed in **Fig. 3e**.

To bridge local optical properties with macroscopic device performance, we perform absolute PL imaging on complete solar cells under 1-sun equivalent illumination, both at open-circuit (OC) and short-circuit (SC) conditions (**Methods**). At OC, the MACl + $PbCl_2$ device exhibits a higher mean QFLS (1.16 eV) compared to 1.12 V for the control device (**Fig. 3e, f**). This aligns with the PLQY data and suggests that the MACl + $PbCl_2$ device exhibits improved luminescence quality over millimetre length scales. We note that a reduced surface energy level mismatch from the UPS data may also contribute to the increased iV_{OC}[60,61]. At SC, devices with higher charge extraction efficiency should exhibit lower PL signals[61,62]. Therefore, comparing the QFLS maps at OC and SC allows us to spatially resolve the charge collection quality (Q_{coll}) of the solar cells[62]. We observe that the control device displays more inhomogeneities, resulting in an approximate Q_{coll} of 85%. In comparison, the MACl + $PbCl_2$ device shows more uniform morphology, achieving an increased Q_{coll} of about 95%. These findings align closely with the CL analysis, underscoring that enhanced luminescence uniformity in MACl + $PbCl_2$ films promotes efficient charge extraction and higher achievable device V_{OC}.

Photovoltaic performance

To evaluate the impact of chloride additives on the photovoltaic performance, we fabricate p-i-n PSCs with the architecture of FTO/NiO_x/2PACz:Me-4PACz/perovskite/C_{60}/SnO_x/Ag (**Fig. 4a**). The thickness of the perovskite layer is approximately 1 µm. Statistical analysis of 20 devices prepared in the same batch indicates a notable increase in PCE, rising from 23.5 ± 0.5% (control) to 25.3 ± 0.2 ($PbCl_2$-treated) and further to 26.3 ± 0.2% (MACl + $PbCl_2$-treated) (**Fig. 4b**). Correspondingly, both the averaged V_{OC} and FF are improved from 1.11 V (control) to 1.16 ($PbCl_2$) and 1.18 V (MACl + $PbCl_2$), and

from 0.79 (control) to 0.82 ($PbCl_2$) and 0.84 (MACl + $PbCl_2$), respectively (**Supplementary Fig. 27**). The enhancement in FF can be attributed to reduced transport losses, compared to the resistance-free pseudo-FF values (**Fig. 3d** and **Supplementary Table 5**). We attribute the superior photovoltaic performance of the MACl + $PbCl_2$ devices to enhanced film uniformity and efficient charge extraction across micro- to millimetre scale dimensions. We note that the change in bandgap due to the chloride addition (20 meV, **Supplementary Fig. 8**) is modest compared to the substantial V_{OC} increase in the $PbCl_2$ and MACl + $PbCl_2$ treated devices. Interestingly, devices treated solely with MACl show limited performance gains despite improved film crystallinity. As shown in the UPS data (**Fig. 2d**), a cliff-like band alignment between the MACl perovskite and C_{60} may facilitate electron transfer but can lower the V_{OC} due to increased interfacial non-radiative recombination[63]. In contrast, for $PbCl_2$, a moderate spike-like offset with C_{60} can help suppress recombination by blocking the backward flow of injected electrons while still allowing for efficient carrier extraction[64,65]. In our case, films made with only MACl also show increased roughness and local heterogeneity, which exacerbates interface-limited losses in the p-i-n architecture. To disentangle the specific role of additional MA and Pb cation from chloride effects, we fabricate reference devices incorporating 13 mol% MAI, 3 mol% PbI_2, or their combination (13 mol% MAI + 3 mol% PbI_2), relative to Pb (**Supplementary Fig. 28**). We find that individual addition of MAI or PbI_2 adversely affects device performance; only their combination slightly increases the PCE from 23.1 ± 0.2% (control) to 24.1 ± 0.4%. These results confirm that performance gains primarily result from chloride incorporation rather than additional MA or Pb cations.

As a result, the optimised MACl + $PbCl_2$ device exhibits a maximum PCE of 27.1% (0.05 cm^2) and features a V_{OC} of 1.185 V, a FF of 0.858, and a J_{SC} of 26.6 mA cm^{-2}, with minimal hysteresis (**Fig. 4c**). The corresponding 1 cm^2 device exhibits a maximum PCE of 25.5%, with a V_{OC} of 1.172 V, a FF of 0.816, and a J_{SC} of 26.7 mA cm^{-2}, with minimal hysteresis. Certified quasi-steady state (QSS) efficiencies of 26.4% and 24.5% are obtained for device areas of 0.05 and 1 cm^2, respectively, validated by the National Photovoltaic Industry Measurement and Testing Center (NPVM) (**Fig. 4d** and **Supplementary Fig. 29–30**). Furthermore, accelerated durability tests (ISOS-D-2I) at elevated temperatures show enhanced stability for encapsulated MACl + $PbCl_2$ devices, retaining over 96% of initial performance after 1200 h at 85 °C, compared to 90% for control devices. Additionally, under continuous maximum power point (MPP) operation at 65 °C and ~50% relative

humidity, MACl + $PbCl_2$-treated devices maintain 88% of initial PCE after 1200 hours, significantly outperforming control devices (78% retention). The enhanced stability of MACl + $PbCl_2$ devices can be attributed to the improved phase purity and more uniform optoelectronic properties of the perovskite absorber[40]. Chloride additives help accelerate the transition from the yellow 2H to more stable 3D phase. In our case, they also improve film crystallinity, luminescence uniformity, and vertical charge transport. These improvements are expected to reduce local recombination centres and suppress interfacial charge accumulation during operation, which can otherwise lead to ion migration and degradation under thermal and light stress. This interpretation is consistent with recent research indicating that optimising the chloride distribution can enhance both device performance and operational stability[52].

We would like to point out that chloride-containing additives cover a diverse range of chemical options, and in many cases, the accompanying cation can influence crystallisation and interfacial chemistry beyond merely supplying Cl^- ions. In this study, we select MACl and $PbCl_2$ as model systems because they are among the most commonly used chloride additives across p-i-n and n-i-p device architectures. This allows us to compare different pathways for chloride incorporation without introducing extra functionalities and perovskite phases. Our findings indicate that beyond MA^+, substituting larger organic ammonium cations, such as propylammonium (PA^+)[44] and phenethylammonium (PEA^+), leads to decreased performance in our p-i-n devices (**Supplementary Fig. 31**). This correlates with a greater tendency to form mixed reduced-dimensional perovskite phases, which can hinder charge collection[66]. Despite this, our findings indicate that Cl^- anions generally lead to better device performance in compared to I^- anions. These results underscore that while Cl^- typically has a beneficial effect on enhancing the quality of the perovskite absorber, the molecular structure of the cation becomes crucial when it leads to the formation of lower-dimensional perovskites.

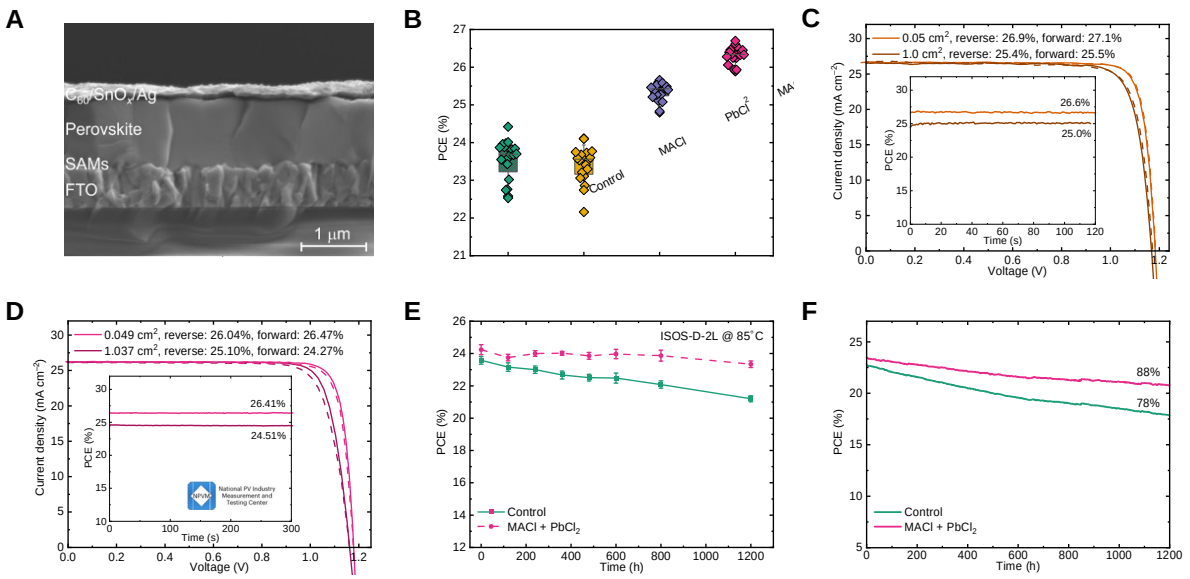

Fig. 4 Photovoltaic and stability performance of PSCs. a, Cross-sectional SEM of a p-i-n cell stack. The scale bar is 1 μm. **b**, PCE statistics (reverse scan) for 20 control, MACl, $PbCl_2$, and MACl + $PbCl_2$ added devices. **c**,**d**, *J*–*V* curve of the champion devices (~0.05 or 1.0 cm^2) measured in-lab and at the National PV Industry Measurement and Testing Center. The insets display steady-state PCEs under MPPT. **e**, ISOS-D-2L device stability during storage at 85 ℃. Statistics are taken from 8 devices for each condition. **f**, MPP stability tracking of the encapsulated device under simulated 1-sun illumination at 65 ℃.

Conclusion

In this study, we elucidated the critical role of chloride-based additives in controlling phase uniformity, compositional homogeneity, and luminescence properties of perovskite films, revealing their significant influence on photovoltaic device performance. We demonstrated that MACl additives increase compositional heterogeneity, causing spatially nonuniform carrier dynamics within perovskite grains. Conversely, $PbCl_2$ proved more effective in homogenising local optoelectronic properties across the films but introduced undesirable PbI_2 phases, detrimental to efficient charge extraction. Importantly, the strategic combination of MACl and $PbCl_2$ enabled optimal crystallinity and uniform carrier dynamics extending from the microscale to millimetre-scale regions. Consequently, this approach significantly reduced interfacial recombination losses, enabling efficient charge-carrier extraction and achieving exceptionally high photovoltaic performance.

Although the chloride additives investigated here are standard in perovskite photovoltaics, our study offers new mechanistic insights by distinguishing the impacts of these commonly used additives. We reveal that the different forms of chloride additives introduce unique pathways for enhancing perovskite film quality, emphasising the importance of additive form and combination strategies. Our findings underscore the possibility of achieving exceptionally high efficiencies using widely accessible additives, thus opening new avenues for further optimisation and scalable deployment of high-performance perovskite solar cells.

Data Availability Statement

The raw data for this article is available on Oxford University Research Archive, at https://ora.ox.ac.uk.

Supplementary information

The Supporting Information is available free of charge at: https://pubs.acs.org/doi/

Materials, experimental methods, and additional device statistics, in-situ PL, XRD, XPS, ToF-SIMS, UPS, CL, TRPL analysis, and solar cell certification reports

Author Information

Corresponding Authors

Hao Chen – *Centre of Future Photovoltaics Research, Global Institute of Future Technology, Shanghai Jiao Tong University, Shanghai 200240, China*; Email: hao.chen1@sjtu.edu.cn

Henry J. Snaith – *Clarendon Laboratory, Department of Physics, University of Oxford, Parks Road, Oxford OX1 3PU, United Kingdom*; Email: henry.snaith@physics.ox.ac.uk

Atsushi Wakamiya – *Institute for Chemical Research, Kyoto University, Gokasho, Uji, Kyoto 611-0011, Japan*; Email: wakamiya@scl.kyoto-u.ac.jp

Zhijun Ning – *School of Physical Science and Technology, ShanghaiTech University, Shanghai 201210, China*; Email: ningzhj@shanghaitech.edu.cn

Authors

Junke Wang – *Clarendon Laboratory, Department of Physics, University of Oxford, Parks Road, Oxford OX1 3PU, United Kingdom*

Shuaifeng Hu – *Clarendon Laboratory, Department of Physics, University of Oxford, Parks Road, Oxford OX1 3PU, United Kingdom*

Xinyu Gu – *Centre of Future Photovoltaics Research, Global Institute of Future Technology, Shanghai Jiao Tong University, Shanghai 200240, China*

Minh Anh Truong – *Institute for Chemical Research, Kyoto University, Gokasho, Uji, Kyoto 611-0011, Japan*

Yi Yang – *Institute of Chemical Sciences and Engineering, École Polytechnique Fédérale de Lausanne, EPFL VALAIS, Sion 1951, Switzerland*

Cheng Liu – *Institute of Chemical Sciences and Engineering, École Polytechnique Fédérale de Lausanne, EPFL VALAIS, Sion 1951, Switzerland*

Gunnar Kusch – *Department of Materials Science and Metallurgy, University of Cambridge, Cambridge CB3 0FS, United Kingdom*

Zhongcheng Yuan – *Clarendon Laboratory, Department of Physics, University of Oxford, Parks Road, Oxford OX1 3PU, United Kingdom*

Manuel Kober-Czerny – *Clarendon Laboratory, Department of Physics, University of Oxford, Parks Road, Oxford OX1 3PU, United Kingdom*

Zuhong Zhang – *Key Lab for Special Functional Materials of Ministry of Education, School of Nanoscience and Materials Engineering, Henan University, Kaifeng 475004, China*

Zhenhuang Su – *Shanghai Synchrotron Radiation Facility, Shanghai Advanced Research Institute, Chinese Academy of Sciences, 239 Zhangheng Road, Shanghai 201204, China*

Kyohei Nakano – *RIKEN Centre for Emergent Matter Science (CEMS), Wako, Saitama 351-0198, Japan*

Akash Dasgupta – *Clarendon Laboratory, Department of Physics, University of Oxford, Parks Road, Oxford OX1 3PU, United Kingdom*

Xianfu Zhang – *Institute of Chemical Sciences and Engineering, École Polytechnique Fédérale de Lausanne, EPFL VALAIS, Sion 1951, Switzerland*

Xinyi Shen – *Clarendon Laboratory, Department of Physics, University of Oxford, Parks Road, Oxford OX1 3PU, United Kingdom*

Nobutaka Shioya – *Institute for Chemical Research, Kyoto University, Gokasho, Uji, Kyoto 611-0011, Japan*

Noriko Kurose – *RIKEN Center for Advanced Photonics (RAP), 2-1, Wako-shi, Saitama 351-0198, Japan*

Daichi Shirakura – *Surface Science Laboratories, Toray Research Centre, Inc., 3-3-7, Sonoyama, Otsu, Shiga 520-8567, Japan*

Zaiwei Wang – *Institute of Technology for Carbon Neutrality, Shenzhen Institute of Advanced Technology, Chinese Academy of Sciences, Shenzhen 518055, China*

Wei Zhou – *School of Physical Science and Technology, ShanghaiTech University, Shanghai 201210, China*

Meng Li – *Key Lab for Special Functional Materials of Ministry of Education, School of Nanoscience and Materials Engineering, Henan University, Kaifeng 475004, China*

Takeshi Hasegawa – *Institute for Chemical Research, Kyoto University, Gokasho, Uji, Kyoto 611-0011, Japan*

Xingyu Gao – *Shanghai Synchrotron Radiation Facility, Shanghai Advanced Research Institute, Chinese Academy of Sciences, 239 Zhangheng Road, Shanghai 201204, China*

Keisuke Tajima – *RIKEN Centre for Emergent Matter Science (CEMS), Wako, Saitama 351-0198, Japan*

Rachel A. Oliver – *Department of Materials Science and Metallurgy, University of Cambridge, Cambridge CB3 0FS, United Kingdom*

Yixin Zhao – *Centre of Future Photovoltaics Research, Global Institute of Future Technology, Shanghai Jiao Tong University, Shanghai 200240, China*

Complete contact information is available at:

https://pubs.acs.org/

Author Contributions

[#]J.W., S.H., X.Gu, M.A.T., and Y.Y. contributed equally to this work.

Notes

H.J.S. is the co-founder and CSO of Oxford PV Ltd. A.W. is the co-founder and CSO of Enecoat Technologies Co., Ltd. All other authors declare no competing interests.

Acknowledgements

We acknowledge the Engineering and Physical Sciences Research Council (EPSRC), UK, under grant numbers EP/S004947/1, EP/X038777/1, and EP/T028513/1, the Marie Skłodowska Curie Actions Postdoc Fellow (UKRI Guarantee, grant numbers EP/Y029216/1 and EP/Y029135/1), NEDO-GI (JPNP21016), NEDO (JPNP20015), JST-MIRAI (JPMJMI22E2), KAKENHI (JP24H00481), and International Collaborative Research Program of ICR, Kyoto University, and the Grant-in-Aid for Scientific Research (B) (JP24K01571) for funding. We thank the National Thin Film Cluster Facility for Advanced Functional Materials (NTCF) at the Department of Physics, University of Oxford, which has been funded by EPSRC (EP/M022900/1) and the Wolfson Foundation. R.A.O. and G.K. acknowledge financial support from the EPSRC under EP/R025193/1. M.K.C. express his gratitude to the Deutsche Forschungsgemeinschaft for financial support via the SPP2196 Priority Program (CH 1672/3-1). A.D. would like to thank the Penrose Scholarship for funding his studentship. H.C. acknowledges the Start-up Fund from Shanghai Jiao Tong University (Grant No. WH220449011) and Shanghai Magnolia Tatent Plan-Pujiang Project (Grant No. BI4900010).

References

1. Kojima, A., Teshima K., Shirai Y., Miyasaka T. Organometal Halide Perovskites as Visible-Light Sensitizers for Photovoltaic Cells. *J. Am. Chem. Soc.* **131**, 6050–6051 (2009).
2. Lee, M. M., Teuscher J., Miyasaka T., Murakami T. N., Snaith H. J. Efficient Hybrid Solar Cells Based on Meso-Superstructured Organometal Halide Perovskites. *Science* **338**, 643–647 (2012).
3. Liu, M., Johnston M. B., Snaith H. J. Efficient planar heterojunction perovskite solar cells by vapour deposition. *Nature* **501**, 395–398 (2013).
4. Malinkiewicz, O., et al. Perovskite solar cells employing organic charge-transport layers. *Nat. Photonics* **8**, 128–132 (2014).
5. De Wolf, S., et al. Organometallic Halide Perovskites: Sharp Optical Absorption Edge and Its Relation to Photovoltaic Performance. *J. Phys. Chem. Lett.* **5**, 1035–1039 (2014).
6. Stranks, S. D., et al. Electron-Hole Diffusion Lengths Exceeding 1 Micrometer in an Organometal Trihalide Perovskite Absorber. *Science* **342**, 341–344 (2013).
7. Stranks, S. D., Snaith H. J. Metal-halide perovskites for photovoltaic and light-emitting devices. *Nat. Nanotech.* **10**, 391–402 (2015).
8. Green, M. A., et al. Solar cell efficiency tables (Version 64). *Prog. Photovolt. Res. Appl.* **32**, 425–441 (2024).
9. NREL Chart, https://www.nrel.gov/pv/assets/pdfs/best-research-cell-efficiencies.pdf. (August 2023).
10. Liu, S., et al. Buried interface molecular hybrid for inverted perovskite solar cells. *Nature* **632**, 536–542 (2024).
11. Chen, H., et al. Improved charge extraction in inverted perovskite solar cells with dual-site-binding ligands. *Science* **384**, 189–193 (2024).
12. Wu, H., et al. Silicon heterojunction back contact solar cells by laser patterning. *Nature* **635**, 604–609 (2024).
13. Lin, H., et al. Silicon heterojunction solar cells with up to 26.81% efficiency achieved by electrically optimized nanocrystalline-silicon hole contact layers. *Nat. Energy* **8**, 789–799 (2023).
14. Stolterfoht, M., et al. The impact of energy alignment and interfacial recombination on the internal and external open-circuit voltage of perovskite solar cells. *Energy Environ. Sci.* **12**, 2778–2788 (2019).
15. Wolff, C. M., Caprioglio P., Stolterfoht M., Neher D. Nonradiative Recombination in Perovskite Solar Cells: The Role of Interfaces. *Adv. Mater.* **31**, 1902762 (2019).
16. Warby, J., et al. Understanding Performance Limiting Interfacial Recombination in pin Perovskite Solar Cells. *Adv. Energy Mater.* **12**, 2103567 (2022).
17. Truong, M. A., et al. Tripodal Triazatruxene Derivative as a Face-On Oriented Hole-Collecting Monolayer for Efficient and Stable Inverted Perovskite Solar Cells. *J. Am. Chem. Soc.* **145**, 7528–7539 (2023).
18. Liu, C., et al. Bimolecularly passivated interface enables efficient and stable inverted perovskite solar cells. *Science* **382**, 810–815 (2023).
19. Yang, Y., et al. Amidination of ligands for chemical and field-effect passivation stabilizes perovskite solar cells. *Science* **386**, 898–902 (2024).
20. Hu, S., et al. Optimized carrier extraction at interfaces for 23.6% efficient tin–lead perovskite solar cells. *Energy Environ. Sci.* **15**, 2096–2107 (2022).
21. Chen, H., et al. Regulating surface potential maximizes voltage in all-perovskite tandems. *Nature* **613**, 676–681 (2023).
22. Lin, Y.-H., et al. Bandgap-universal passivation enables stable perovskite solar cells with low photovoltage loss. *Science* **384**, 767–775 (2024).

23. Hu, S., Thiesbrummel J., Pascual J., Stolterfoht M., Wakamiya A., Snaith H. J. Narrow Bandgap Metal Halide Perovskites for All-Perovskite Tandem Photovoltaics. *Chem. Rev.* **124**, 4079-4123 (2024).
24. Hu, S., et al. A Universal Surface Treatment for p–i–n Perovskite Solar Cells. *ACS Appl. Mater. Interfaces* **14**, 56290–56297 (2022).
25. Al-Ashouri, A., et al. Monolithic perovskite/silicon tandem solar cell with >29% efficiency by enhanced hole extraction. *Science* **370**, 1300–1309 (2020).
26. de Quilettes, D. W., et al. Impact of microstructure on local carrier lifetime in perovskite solar cells. *Science* **348**, 683−686 (2015).
27. Macpherson, S., et al. Local nanoscale phase impurities are degradation sites in halide perovskites. *Nature* **607**, 294–300 (2022).
28. Correa-Baena, J.-P., et al. Homogenized halides and alkali cation segregation in alloyed organic-inorganic perovskites. *Science* **363**, 627–631 (2019).
29. Frohna, K., et al. The impact of interfacial quality and nanoscale performance disorder on the stability of alloyed perovskite solar cells. *Nat. Energy* **10**, 66–76 (2024).
30. Datta, K., et al. Local halide heterogeneity drives surface wrinkling in mixed-halide wide-bandgap perovskites. *Nat. Commun.* **16**, 1967 (2025).
31. Liang, Z., et al. Homogenizing out-of-plane cation composition in perovskite solar cells. *Nature* **624**, 557–563 (2023).
32. Wang, J., et al. Halide homogenization for low energy loss in 2-eV-bandgap perovskites and increased efficiency in all-perovskite triple-junction solar cells. *Nat. Energy* **9**, 70–80 (2024).
33. Wang, X., et al. Regulating phase homogeneity by self-assembled molecules for enhanced efficiency and stability of inverted perovskite solar cells. *Nat. Photonics* **18**, 1269–1275 (2024).
34. Hao, M., et al. Nanoscopic cross-grain cation homogenization in perovskite solar cells. *Nat. Nanotech.* **20**, 630–638 (2025).
35. Luo, X., et al. Effects of local compositional heterogeneity in mixed halide perovskites on blue electroluminescence. *Matter* **7**, 1054−1070 (2024).
36. Liu, X., Guo Y., Cheng Y., Lu S., Li R., Chen J. Advances in chloride additives for high-efficiency perovskite solar cells: multiple points of view. *Chem. Commun.* **59**, 13394–13405 (2023).
37. Lim, J., et al. Benign methylformamidinium byproduct induced by cation heterogeneity inhibits local formation of δ-phase perovskites. *Energy Environ. Sci.* **17**, 9134–9143 (2024).
38. Wehrenfennig, C., Eperon G. E., Johnston M. B., Snaith H. J., Herz L. M. High Charge Carrier Mobilities and Lifetimes in Organolead Trihalide Perovskites. *Adv. Mater.* **26**, 1584–1589 (2014).
39. Shen, X., et al. Chloride-Based Additive Engineering for Efficient and Stable Wide-Bandgap Perovskite Solar Cells. *Adv. Mater.* **35**, 2211742 (2023).
40. Kim, M., et al. Methylammonium Chloride Induces Intermediate Phase Stabilization for Efficient Perovskite Solar Cells. *Joule* **3**, 2179–2192 (2019).
41. Qin, M., et al. Manipulating the Mixed-Perovskite Crystallization Pathway Unveiled by In Situ GIWAXS. *Adv. Mater.* **31**, 1901284 (2019).
42. Zhang, Y., et al. Nonalloyed α-phase formamidinium lead triiodide solar cells through iodine intercalation. *Science* **387**, 284–290 (2025).
43. Li, H., et al. Sequential vacuum-evaporated perovskite solar cells with more than 24% efficiency. *Sci. Adv.* **8**, eabo7422 (2022).
44. Park, J., et al. Controlled growth of perovskite layers with volatile alkylammonium chlorides. *Nature* **616**, 724–730 (2023).
45. Lu, H., et al. Vapor-assisted deposition of highly efficient, stable black-phase $FAPbI_3$ perovskite solar cells. *Science* **370**, eabb8985 (2020).

46. Wang, M., et al. Accelerating direct formation of α-FAPbI3 by dual-additives synergism for inverted perovskite solar cells with efficiency exceeding 26%. *Chem. Eng. J.* **505**, 159056 (2025).
47. Pham, N. D., et al. Enhanced perovskite electronic properties via a modified lead(ii) chloride Lewis acid–base adduct and their effect in high-efficiency perovskite solar cells. *J. Mater. Chem. A* **5**, 5195–5203 (2017).
48. Jiang, F., et al. Synergistic Effect of PbI_2 Passivation and Chlorine Inclusion Yielding High Open-Circuit Voltage Exceeding 1.15 V in Both Mesoscopic and Inverted Planar $CH_3NH_3PbI_3$(Cl)-Based Perovskite Solar Cells. *Adv. Funct. Mater.* **26**, 8119–8127 (2016).
49. Liu, M., Johnston M. B., Snaith H. J. Efficient planar heterojunction perovskite solar cells by vapour deposition. *Nature* **501**, 395-398 (2013).
50. Xu, J., et al. Triple-halide wide-band gap perovskites with suppressed phase segregation for efficient tandems. *Science* **367**, 1097–1104 (2020).
51. Chen, S., et al. Crystallization in one-step solution deposition of perovskite films: Upward or downward? *Sci. Adv.* **7**, eabb2412 (2021).
52. Xiong, Z., et al. Homogenized chlorine distribution for >27% power conversion efficiency in perovskite solar cells. *Science* **390**, 638–642 (2025).
53. Nakamura, T., et al. Sn(IV)-free tin perovskite films realized by in situ Sn(0) nanoparticle treatment of the precursor solution. *Nat. Commun.* **11**, 3008 (2020).
54. Li, W., et al. Phase Segregation Enhanced Ion Movement in Efficient Inorganic $CsPbIBr_2$ Solar Cells. *Adv. Energy Mater.* **7**, 1700946 (2017).
55. Ferrer Orri, J., et al. Using pulsed mode scanning electron microscopy for cathodoluminescence studies on hybrid perovskite films. *Nano Express* **2**, 024002 (2021).
56. Rack, P. D., Peak J. D., Melcher C. L., Fitz-Gerald J. M. Scanning electron and cathodoluminescence imaging of thin film Lu_2SiO_5:Ce scintillating materials. *Appl. Phys. Lett.* **91**, (2007).
57. Singh, R. K., Chen Z., Kumar D., Cho K., Ollinger M. Critical issues in enhancing brightness in thin film phosphors for flat-panel display applications. *Appl. Surf. Sci.* **197-198**, 321–324 (2002).
58. Kober-Czerny, M., et al. Determining Parameters of Metal-Halide Perovskites Using Photoluminescence with Bayesian Inference. *PRX Energy* **4**, 013001 (2025).
59. Cho, C., et al. Efficient vertical charge transport in polycrystalline halide perovskites revealed by four-dimensional tracking of charge carriers. *Nat. Mater.* **21**, 1388–1395 (2022).
60. Liu, Z., Siekmann J., Klingebiel B., Rau U., Kirchartz T. Interface Optimization via Fullerene Blends Enables Open-Circuit Voltages of 1.35 V in CH3NH3Pb(I0.8Br0.2)3 Solar Cells. *Adv. Energy Mater.* **11**, 2003386 (2021).
61. Akel, S., Wang Y., Yan G., Rau U., Kirchartz T. Charge Carrier Collection Losses in Lead-Halide Perovskite Solar Cells. *Adv. Energy Mater.* **n/a**, 2401800 (2024).
62. Dasgupta, A., et al. Visualizing Macroscopic Inhomogeneities in Perovskite Solar Cells. *ACS Energy Lett.* **7**, 2311–2322 (2022).
63. Liu, Z., Siekmann J., Klingebiel B., Rau U., Kirchartz T. Interface Optimization via Fullerene Blends Enables Open-Circuit Voltages of 1.35 V in $CH_3NH_3Pb(I_{0.8}Br_{0.2})_3$ Solar Cells. *Adv. Energy Mater.* **11**, 2003386 (2021).
64. Hu, H., et al. Sn-Pb Mixed Perovskites with Fullerene-Derivative Interlayers for Efficient Four-Terminal All-Perovskite Tandem Solar Cells. *Adv. Funct. Mater.* **32**, 2107650 (2022).
65. Ding, C., et al. Effect of the conduction band offset on interfacial recombination behavior of the planar perovskite solar cells. *Nano Energy* **53**, 17–26 (2018).

66. Chen, H., et al. Quantum-size-tuned heterostructures enable efficient and stable inverted perovskite solar cells. *Nat. Photonics* **16**, 352–358 (2022).

682

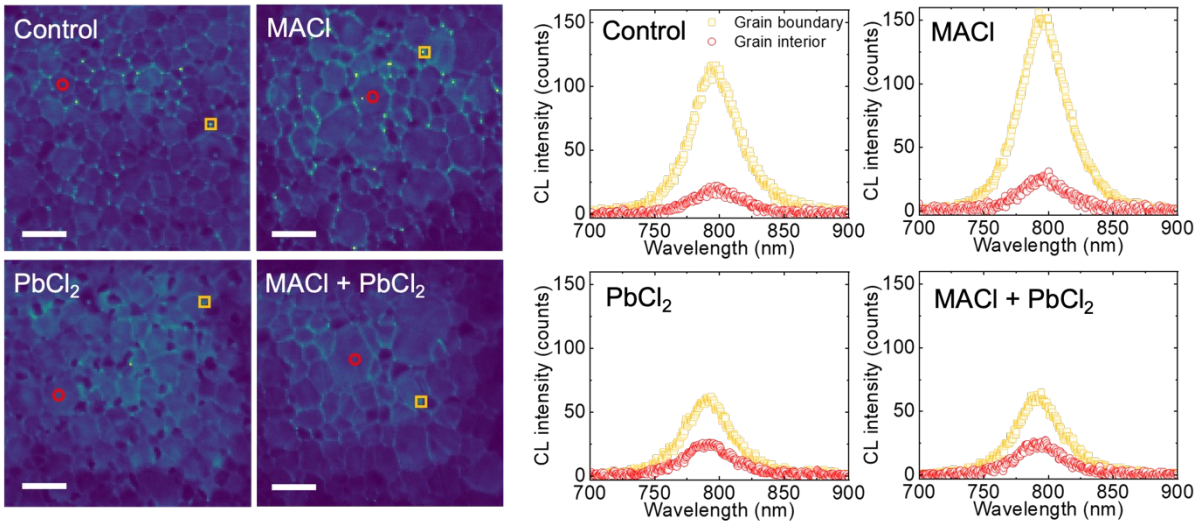

683 (For Table of Contents Only)